An HI Mosaic of the Small Magellanic Cloud

L. Staveley-Smith, R.J. Sault, D. McConnell, M.J. Kesteven

Australia Telescope National Facility, CSIRO, PO Box 76, Epping, NSW 2121

D. Hatzidimitriou

Physics Department, University of Crete, 714.09 Heraklion, Crete, Greece

K.C. Freeman and M.A. Dopita

Mount Stromlo and Siding Spring Observatories, Weston Creek PO, Canberra, ACT 2611

Abstract: This paper describes the first results from a 20 deg^2 mosaic of the Small Magellanic Cloud (SMC) in the λ21-cm line of neutral hydrogen. The mosaic consists of 320 separate pointings with the 375-m array of the Australia Telescope Compact Array. The angular resolution is $1'.5$ (26 pc, for a distance of 60 kpc) and the velocity resolution is 1.6 km s^{-1}. The images reveal a structure of remarkable complexity, with much of the spatial power contained in high brightness temperature compact knots and filaments. Numerous wind-blown 'bubbles' and 'supershells' are evident in the data, both inside and outside the stellar confines of the SMC. Some high-density HI regions are seen to correlate with Hα regions, indicating sites of current star formation. However, many high-column-density HI regions are devoid of optical emission and may represent regions of future star formation. These regions may be underabundant in diffuse molecular gas due to the high radiation field and low metallicity of the SMC.

1. Introduction

The SMC is one of our nearest extragalactic neighbours and is distinguished as being amongst the most chemically young and gas-rich galaxies known. The evolution of the SMC is intimately connected with that of its neighbour, the Large Magellanic Cloud (LMC) with which it appears to have had a recent encounter (Murai and Fujimoto 1980; Gardiner *et al.* 1994) leaving a gaseous (McGee and Newton 1981) and stellar (Irwin 1991) trail stretching between the two galaxies. HI maps of the SMC include those published by Hindman (1967), McGee and Newton (1981) and Mathewson *et al.* (1988). These studies have benefited from improvements in sensitivity and velocity resolution with time. However, all have been limited by the relatively poor spatial resolution (260 pc) afforded by the Parkes telescope at λ21 cm. This makes it difficult to perform a detailed multi-wavelength comparison with the various other components of the ISM. For example, the recent CO maps from the SEST telescope (e.g. Rubio *et al.* 1993) have a spatial resolution of 13 pc.

The advent of the Australia Telescope Compact Array (ATCA) (The Australia Telescope 1992), has changed this with even the most compact imaging array offering an order of magnitude improvement in spatial resolution over the Parkes telescope. We have therefore imaged the main body of the SMC, covering an area of about 20 deg^2 with the ATCA. In this paper, we present an overview of the observations and data reduction (Section 2) and a selection of some of the results (Section 3). We point out that this data is available to the astronomical community (details in Section 4).

2. Observations and Data Reduction

The observations were taken over eight days from 1992 October 6 to 1992 October 14 (October 8 was lost due to high wind). The 375-m configuration[1] of the ATCA was used. The observation bandwidth of 4 MHz (844 km s^{-1}) was divided into 1024 channels, resulting in a channel spacing of 0.82 km s^{-1}. Disk-space limitations necessitated averaging adjacent channels in the imaging procedure, resulting in a final velocity resolution of 1.6 km s^{-1}. The central observing frequency was set at 1420 MHz, corresponding to a recession velocity of 86 km s^{-1}. Both linear polarization channels were used.

The observations were taken in a 'mosaicing' mode which was initially developed for this project, but is now available as a standard ATCA observing mode. On each day, 40 fields were observed. To maximize *uv*-coverage, each field was observed for 16.1 s, and 3.9 s were allowed for the antennas to drive to an adjacent field. The distribution of the fields on the sky shown in Fig. 1 was based on previous Parkes observations (Hindman 1967; McGee and Newton 1981). Each mosaic pattern was executed three times (a total of 40 min), after which a short observation of the phase and amplitude calibrator, PKS B0252–712, was made. This procedure was repeated continuously throughout the day. For each of the 320 fields, a minimum of 12 h (non-continuous) *uv*-coverage was obtained with an effective integration time of $\sim$ 15 min per field. A typical *uv*-coverage is shown in Fig. 2.

The fields were spaced in a hexagonal grid (see Fig. 1) of side $15'$. This spacing was smaller than necessary for Nyquist sampling at 1.4 GHz because we took simultaneous wideband continuum observations at 2.4 GHz (this continuum data and the 1.4 GHz continuum data from the line-free channels will be discussed in a later paper). The observing procedure ensured full sampling

[1] The '375-m array' has a baseline coverage, in increments of 15.3 m, of 2, 4, 6, 8, 12, 14, 16, 18, 22 and 30 units

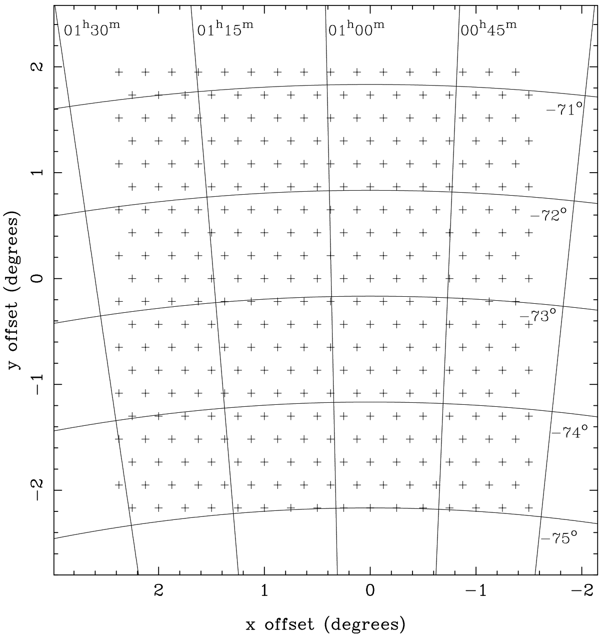

Figure 1: Distribution on the sky of the 320 pointings of the Compact Array used to mosaic the SMC. A J2000 coordinate grid is overlaid on the tangent-plane grid used here. Equal time was spent at each position. The FWHP primary beam of the 22-m Compact Array antennas is $34'$ at 1.42 GHz.

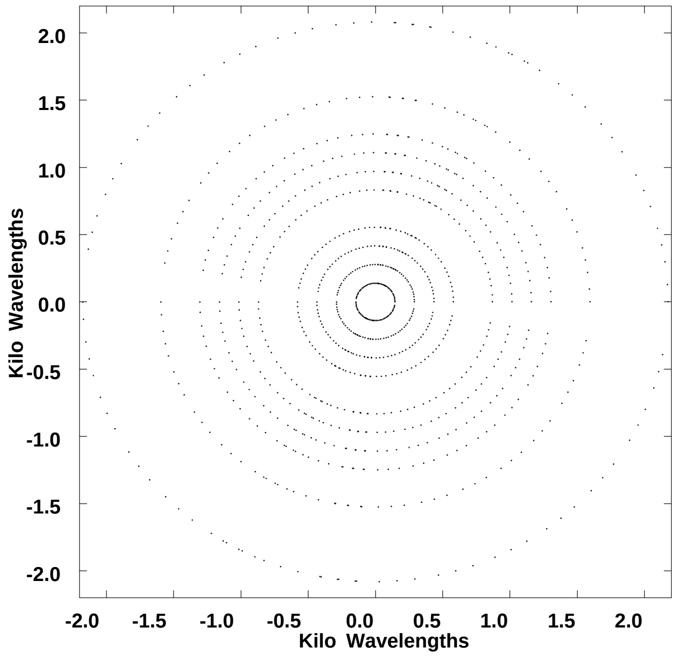

Figure 2: A typical coverage of the uv-plane for the SMC survey. This plot is for field 111, which lies close to the central position.

of the uv-plane in the tangential direction, except for the longest baselines. Sampling in the radial direction was not quite as good, although the process of combining neighbouring pointings reduces the radial gaps to only $\sim 35\%$ of the total uv-area (Ekers and Rots 1979; Cornwell et al. 1993). Primary flux density calibration was based on the revised value for PKS B1934–638 of 14.9 Jy at 1420 MHz.

The data were edited and calibrated in `AIPS`. Corrections to the amplitude and phases of only a few percent and a few degrees, respectively, were required owing to the excellent observing conditions. Bandpass calibration using PKS B1934–638 was performed and heliocentric corrections were applied to the uv-data. Cubes and beams for each field were made using `MIRIAD`. The pixel size used was $40''$, and the size of each cube was $128 \times 128 \times 78$ planes, giving a spatial size of $85' \times 85'$ for each field with a velocity range from 88 to 216 km s^{-1}. The data were 'uniformly' weighted, resulting in a theoretical noise for each field of ~ 45 mJy beam^{-1}. To avoid some of the geometrical gridding and deconvolution problems arising from the large area surveyed and the southerly declination of the SMC, the data cubes were then shifted onto a tangent plane after Fourier inversion. The cubes were then simultaneously combined and deconvolved using a maximum entropy procedure, as implemented in the `MIRIAD` routine "`mosaic`". The final cube was formed by convolving the maximum entropy model with a Gaussian of FWHM $97''.2 \times 81''.9$ (position angle $-55°$) and folding in the image residuals. The final rms noise of 19 mJy beam^{-1}, measured in line-free parts of the final cube, is close to the estimated theoretical noise of 17 mJy beam^{-1} for the mosaiced data set. This corresponds to a $1-\sigma$ brightness temperature sensitivity of 1.4 K, or a column density sensitivity of 1.3×10^{19} cm^{-2} in the case of a 5-km s^{-1} linewidth and optically thin emission.

3. Results

(a) Isovelocity images

As an example of the quality and wealth of the data in this survey, we present four isovelocity images (channel maps) plotted in grey-scale representation in Fig. 3. The coordinate scale is a J2000 tangent plane centred on $\alpha = 00^{\mathrm{h}}55^{\mathrm{m}}$ $\delta = -72°50'$ (J2000). A coordinate transformation matrix is given in Appendix A. Alternatively, Fig. 1 can be used for transformation. The appropriate heliocentric velocities ($v = c\Delta\lambda/\lambda_\circ$), given in the top left of each plane, are 110, 123.2, 156.1 and 189.1 km s^{-1}. The velocity range in which we find HI emission is 88–216 km s^{-1}.

In these plots, we have suppressed the noise amplification due to the primary beam response. Therefore, features close to the edge of the mosaic will be diminished in amplitude by the weighted primary beam factor. Also, around bright features, there are negative bowls in the data (white areas in Fig. 3). These are common in interferometric images and simply correspond to the presence of large-scale structure which the Compact Array is insensitive to, and has therefore filtered out. In a later paper, we plan to add low-spatial frequencies from single-dish observations to eliminate these negative bowls.

At 110 km s^{-1}, we see a remarkable circular feature at $(x, y) = (-1^\circ.2, -0^\circ.7)$. The diameter of this feature is 0.9 kpc, and its morphology resembles that of a 'supershell' (cf. Heiles 1979). This shell overlaps with the second of Hindman's (1967) three expanding supershells, which lies further to the south. The shell shows a high degree of complexity in the ATCA data, with many high density condensations on its rim. The diffuse HII regions DEM S2 and S13 (Davies *et al.* 1976) are associated with high density HI concentrations and undoubtedly represent regions of secondary star formation. The north-east part of the shell runs into the HII complex in the south-west region of the optical bar (DEM S9–11 and S12–45). The peak brightness temperature is 98 K in this region of the shell. This implies a high kinetic temperature for this gas, or a high optical depth. Parts of the south-west bar region have been mapped in CO by Rubio *et al.* (1993). For the field SMC-B1, containing DEM S16 (or N13A,B; Henize 1956), S21 (N16) and S28 (N15), there are nearby dense HI condensations associated with the rim of the shell. However, the detailed correlation between the low-velocity HI and CO gas is poor below a scale size of 50 pc. For the field SMC-B2 the correlation is good, with the HI following the same ridge line through the HII regions DEM S34–39 as the ^{12}CO(1–0) emission mapped by Rubio *et al.*

A linear feature protrudes from the north-east part of the shell. This feature is parallel to the optical 'bar' of the SMC. The north-eastern end points to another, smaller (diameter 340 pc) ring of HI which again appears to be a shell whose expansion velocity is 21 km s^{-1}. These parameters lead to a dynamical age ($\frac{3}{5}r/v$) of 4×10^6 yr. The HII regions DEM S63, S68 (N50), S77 (N52A,B) and S80 lie near the centre of this shell. They are probably in the background, however, given the heliocentric velocity of 169 km s^{-1} measured by Smith and Weedman (1973) for N50. The HI shell appears to be the apex of a large, low-surface-brightness envelope reminiscent of a bow shock, whose position angle again corresponds to that of the bar.

At 123.2 km s^{-1}, we begin to see a remarkable set of clouds around the SMC. These are possibly shaped by fragmentation of the shock fronts which result from supernovae and stellar winds. No optical counterparts are seen. The column densities ($\sim 10^{20}$ cm^{-2}) and velocity dispersions (~ 2 km s^{-1}) are similar to the high-latitude 'cirrus' clouds in our own Galaxy, though the distance of the SMC ensures that we see only the clouds of larger physical size (~ 100 pc) and mass ($\sim 10^3 M_\odot$) than observed in the Galaxy. We note, however, that no obvious 100-μm emission is present at the position of these clouds in the maps of Schwering and Israel (1990) whereas, based on the Galactic HI/infrared ratio of Boulanger *et al.* (1985), a 100-μm surface brightness value of 1.4 MJy sr^{-1} is expected. This may be the result of low dust content or low temperature in these regions. If the latter, then our mass estimates will be substantially underestimated due to the optical depth of the HI line.

Also at this velocity, an interesting pair of relatively isolated, overlapping shells is evident in the north-west, near $(x, y) = (-1^\circ.2, 1^\circ.6)$. These shells are approximately 550 pc in diameter, and overlap, at least in projection, to form a figure-of-eight. Again, no obvious optical counterpart is present (e.g. Fig. 4b).

At 156 km s^{-1}, emission to the north of the north-eastern part of the bar of the SMC is prominent. Also, emission associated with the eastern 'wing' of the SMC is visible. These are evidently highly complex structures and, as with the previous plane, give the impression of multiple overlapping shell structures resulting from the interaction of supernovae and stellar winds with the ISM. Many of these regions are remote from the main optical body of the SMC.

At 189 km s^{-1}, we see a loop of dense neutral gas at $(x, y) = (2^\circ.1, -1^\circ.4)$. This is associated with the third Hindman (1967) supershell. The major axis of the object is 2.0 kpc in size, but it may be a little larger as the south-east corner falls very close to the edge of the mosaiced region. The elliptical shape of this loop may result from a density gradient along the major axis, rather than a velocity anisotropy in the outflow.

(b) Brightness Temperature Image

A convenient way to represent the overall data cube is by means of a brightness temperature map where, for each spatial position, the peak of the HI spectrum is plotted. This image, together with an Hα line+continuum image (G.D.Bothun, private communication) covering the same region, is shown in Fig. 4. The peak brightness temperature is 131 K at $(x, y) = (-0^\circ.46, -0^\circ.25)$ ($\alpha = 00^{\rm h}48^{\rm m}.7 \quad \delta = -73^\circ 04'$, J2000). The overall HI shape of the SMC is dissimilar to the optical morphology, showing a 'three-armed' structure in contrast to the optical 'bar-plus-wing' morphology. The northern and eastern arms of the HI structure have little in the way of a stellar counterpart. The fine overall filamentary structure of the SMC is remarkable. Undoubtedly, much of this arises from cell walls and shock fronts created by expanding shell structures, but it may be that magnetic forces on charged particles in the denser filaments cause the entrainment of some neutral gas. A detailed comparison with radio continuum images is required here.

4. Data Availability

The data in this paper are available to the astronomical community in various forms, including FITS files and postscript images. Contact Lister Staveley-Smith (e-mail `lstavele@atnf.csiro.au`) for details.

Acknowledgments

We thank Bart Wakker for his assistance with the MIRIAD "mosaic" program, Neil Killeen for the "cgdisp" plotting program, Warwick Wilson for implementing correlator blanking, Robert Braun for discussions on moment analysis, and Greg Bothun for the 'Parking Lot' CCD image.

The Australia Telescope, 1992, *J. Electr. Electron. Eng. Aust.* (special issue), **12**, no. 2, June.
Boulanger, F., Baud, B. and van Albada, G.D., 1985, *A&A*, **144**, L9.
Cornwell, T.J., Holdaway, M.A. and Uson, J.M., 1993, *A&A*, **271**, 697.
Davies, R.D., Elliott, K.H. and Meaburn, J., 1976, *Mem. R. astr. Soc.*, **81**, 89.
Ekers, R.D. and Rots, A.H., 1979, In *Image Formation from Coherence Functions in Astronomy*, IAU Colloq. 49, C. van Schooneveld (ed.), p. 61.
Gardiner, L.T., Sawa, T. and Fujimoto, M., 1994, *MNRAS*, **266**, 567.
Heiles, C., 1979, *ApJ*, **229**, 533.
Henize, K.G., 1956, *ApJS*, **2**, 315.
Hindman, J.V., 1967, *Aust. J. Phys.*, **20**, 147.
Irwin, M.J., 1991, In *The Magellanic Clouds*, IAU Symposium 148, R.F. Haynes and D.K. Milne (eds), p. 453.
McGee, R.X. and Newton, L.M., 1981, *PASA*, **4**, 189.
Mathewson, D.S., Ford, V.L. and Visvanathan, N., 1988, *ApJ*, **333**, 617.
Murai, T. and Fujimoto, M., 1980, *PASJ*, **32**, 581.
Rubio, M., Lequeux, J., Boulanger, F., Booth, R.S., Garay, G., de Graauw, Th., Israël, F.P., Johansson, L.E.B., Kutner, M.L. and Nyman, L.-A, 1993, *A&A*, **271**, 1.
Schwering, P.B.W. and Israel, F.P., 1990, *Atlas and Catalogue of Infrared Sources in the Magellanic Clouds* (Kluwer).
Smith, M.G. and Weedman, D.W., 1973, *ApJ*, **179**, 461.

Appendix A

The coordinate system used here is based on a tangent point at $\alpha = 00^{\rm h}55^{\rm m}$ $\delta = -72°50'$ (J2000) (of no dynamical significance). The line of zero longitude in this system is defined to coincide with the line of J2000 longitude at $00^{\rm h}55^{\rm m}$.

The following equation was used for the transformation of the J2000 direction cosine vector $\vec{t} = (\cos\alpha\cos\delta, \sin\alpha\cos\delta, \sin\delta)$ to the tangent plane vector $\vec{w} = (\cos x \cos y, \sin x \cos y, \sin y)$:

$$\vec{w} = M\vec{t}. \qquad (1)$$

The transformation matrix M is given by

$$M = \begin{pmatrix} 0.286693843 & 0.070153537 & -0.95545021 \\ -0.237685892 & 0.971342069 & 0.0 \\ 0.928068993 & 0.227097037 & 0.295152297 \end{pmatrix}. \qquad (2)$$

The inverse transformation matrix M^{-1} is the transpose of M.

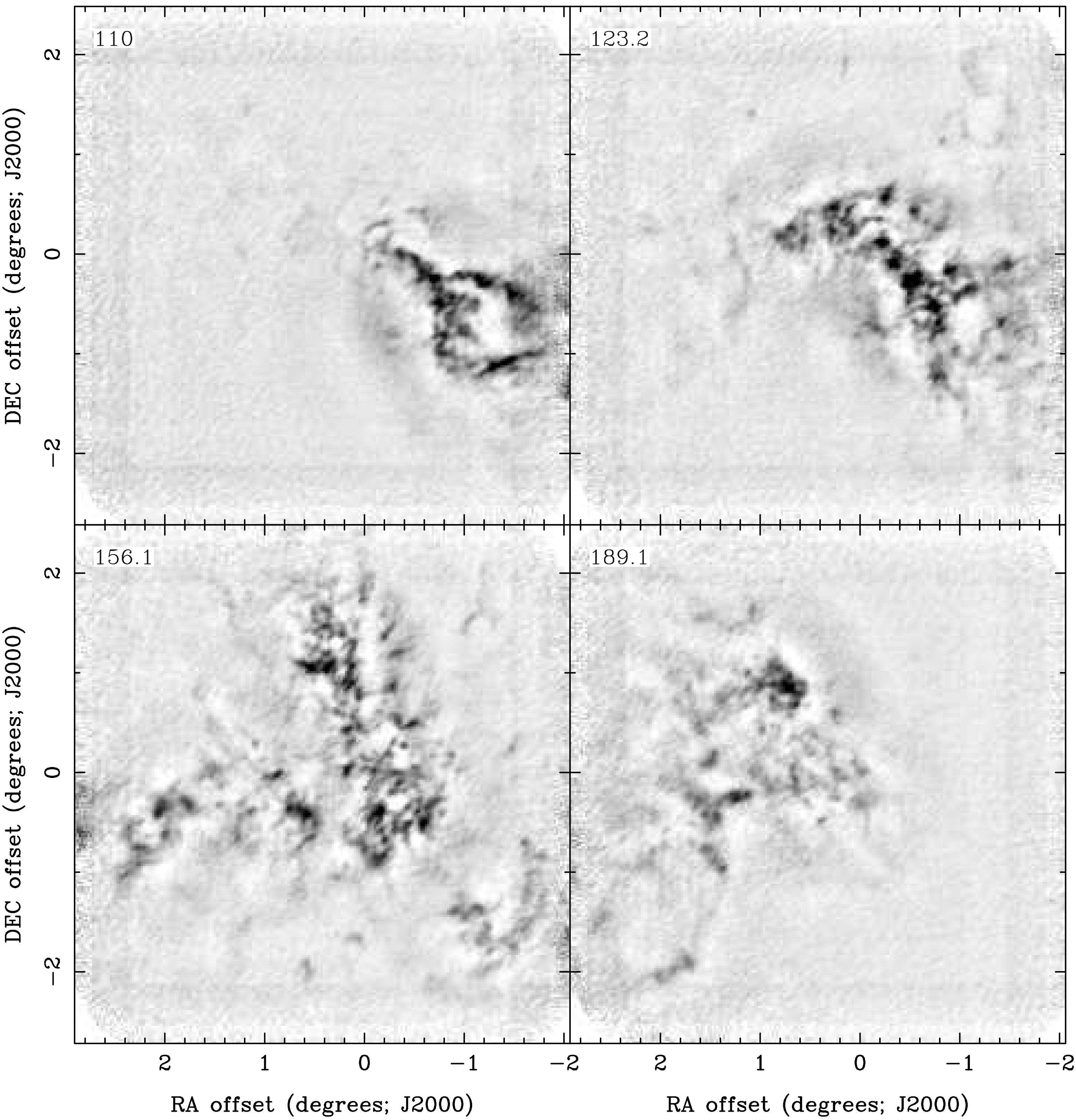

Figure 3: Four planes extracted from the ATCA HI cube of the SMC. Heliocentric velocities are 110, 123.2, 156.2 and 189.1 km s^{-1}.

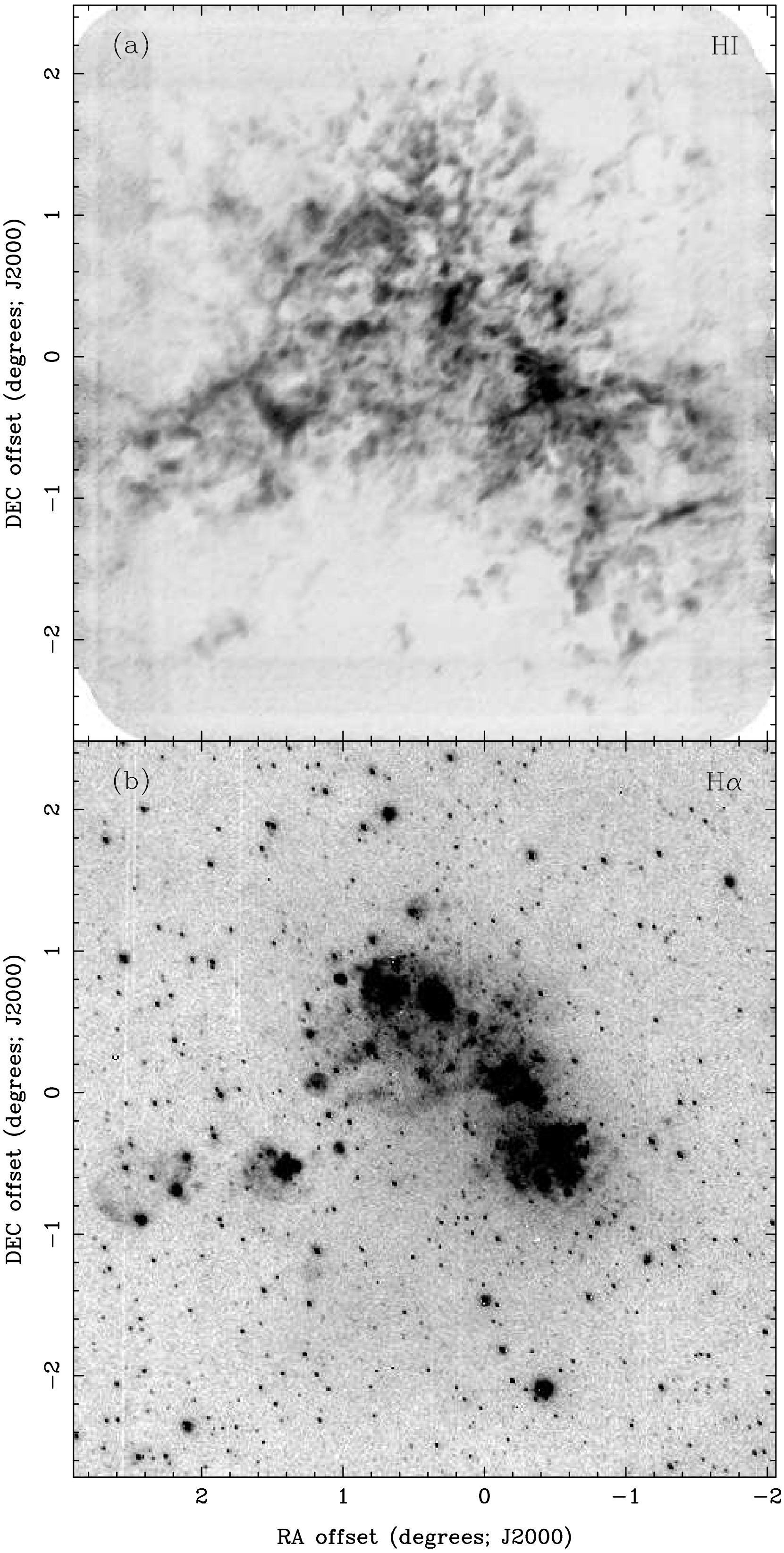

Figure 4: (a) HI image of the SMC showing, for each position, the peak brightness temperature in the HI spectrum; (b) Optical (Hα+ continuum) image of the SMC (G.D. Bothun, private communication).